International Journal of Heat and Mass Transfer 52 (2009) 921–931

Contents lists available at ScienceDirect

International Journal of Heat and Mass Transfer

journal homepage: www.elsevier.com/locate/ijhmt

Large-eddy simulation of an impinging jet in a cross-flow on a heated wall-mounted cube

D. Rundström *, B. Moshfegh

Division of Energy and Mechanical Engineering, Department of Technology and Built Environment, University of Gävle, S-802 62 Gävle, Sweden
Department of Management and Engineering, Linköping Institute of Technology, S-581 83 Linköping, Sweden

ARTICLE INFO

Article history:
Received 20 September 2007
Received in revised form 18 February 2008
Available online 12 September 2008

Keywords:
Large-eddy simulation
Impinging jet in a cross-flow
Reynolds stress model
Electronic cooling

ABSTRACT

A large-eddy simulation (LES) is performed in order to predict the mean velocity field, the turbulence characteristics and the heat transfer rate of an impinging jet in cross-flow configuration on a heated wall-mounted cube. The WALE model was used to model the subgrid-scale tensor. The results from the LES are compared with a Reynolds stress model (RSM) and against earlier measurements with identical set-up. A comparison between the results from the predictions and the measurements shows that in general the LES has better agreement with the measurements compared to the RSM and particularly in the stagnation region of the impinging jet.

1. Introduction

Impinging jets are used for many industrial applications where high heat and/or mass transfer rates are required (e.g., drying paper, textiles, tempering glass and cooling of electronic components). The current trend in the development of electronic devices shows a steady increase in the dissipated heat from electronic components. Forced channel flow is frequently used as a cooling technique, see Meinders [1]. In combating the whole thermal load with forced channel flow, excessive flow rates will be required. One possible method to face this problem is to divide the channel flow with an impinging jet and a low-velocity channel flow, see Rundström and Moshfegh [2].

Impinging jets are also of great scientific interest. Extensive experimental and numerical research has been carried out to predict the flow and heat transfer characteristics in the stagnation region of an impinging jet. Most investigations have been focused on axisymmetric round jets impinging normally on a flat surface, cf. Lee and Lee [3]. The case with an axisymmetric round jet impinging normally on a flat surface has also been simulated with different turbulence models to predict the heat transfer and flow configuration. The earlier investigations by Behnia et al. [4] have shown that the most common two-equation Reynolds Averaged Navier–Stokes (RANS) models, e.g., the standard k-ε model, over-predict the heat transfer rate in the stagnation region by over 100%. Behnia et al. [4] also used the $\overline{v^2}$-f model to simulate the case, with satisfactory agreement with the experimental data. Other numerical investigations, such as the one by Abdon and Sundén [5], have used the expansion of the classical two-equation turbulence models (k-ε and k-ω) with realizable constraints. Craft et al. [6] used a low-Re model with the Yap correlation added to the ε-equation and three different Reynolds stress models to simulate the case.

A range of large-eddy simulations (LES) with different kinds of subgrid-scale (SGS) models have also been used to predict the turbulent flow field near the stagnation point. Beaubert and Viazzo [7] used the dynamic Smagorinsky model by Lilly [8] to simulate a plane impinging jet with three different Reynolds numbers. The mean velocity profiles and the turbulence statistics were in good agreement with the measurements by Maurel and Solliec [9]. Olsson and Fuchs [10] investigated the performance of two SGS models, a modified version of the dynamic model by Lilly [8] and a stress-similarity model by Liu et al. [11]. They found that the SGS models had a significant influence on the flow field especially for the turbulence statistics. They also revealed the importance of forcing the velocity fluctuation at the inlet of the impinging jet. Tsubokura et al. [12] used direct numerical simulation (DNS) and large-eddy simulation (LES) with a dynamic SGS model to investigate the eddy structures of plane and round impinging jets. They found that the eddy structures are different in the stagnation region for plane and round impinging jets. For the plane impinging jets, organized vortex structures were found in the stagnation region such as twin counter-rotating vortices in the transverse direction of the jet; no organized vortex structures were found in

* Corresponding author. Address: Division of Energy and Mechanical Engineering, Department of Technology and Built Environment, University of Gävle, S-802 62 Gävle, Sweden. Tel.: +46 26 64 87 34; fax: +46 26 64 88 28.
E-mail addresses: drm@hig.se (D. Rundström), bahram.moshfegh@liu.se (B. Moshfegh).

0017-9310/$ - see front matter © 2008 Elsevier Ltd. All rights reserved.
doi:10.1016/j.ijheatmasstransfer.2008.03.035

Nomenclature

a_{ij} orthogonal transformation tensor
C_d drag-coefficient
D nozzle diameter
E energy spectrum function
H channel height
h cube height
h_j modified subgrid-scale heat fluxes
k turbulent kinetic energy
L_s, l turbulent length scales
M mean value
N normal distribution and number of samples
Pr_t turbulent Prandtl number
p static pressure
q second invariant of the velocity gradient tensor
$Re_j = U_j D/\nu$ Reynolds number based on the nozzle diameter and the jet velocity
$Re_c = U_c H/\nu$ Reynolds number based on the channel, height and mean velocity in the channel
r normal distance to the closest wall
S_{ij} rate-of-strain tensor
S_x streamwise distance of the computational domain
S_z spanwise distance of the computational domain
T instantaneous temperature
T' fluctuating temperature
t time
U_c mean velocity of the cross-flow
U_j mean velocity of the impinging jet,
$U_i = (UVW)$ time-averaged velocity components
$u_i = (uvw)$ instantaneous velocity components
u_i' fluctuating velocity
V time-averaged y-velocity component and volume of the computational cell
$x_i = (xyz)$ Cartesian coordinates
y^+ distance from the wall normalized by the viscous length scale

Greek symbols
α thermal diffusivity
δ_{ij} Kronecker delta
ε dissipation rate of turbulent kinetic energy
ε_{ijk} permutation tensor
Δt time step size
κ wave-number and van Karman constant
κ_j wave-number vector
ν kinematic viscosity
ζ_{ij} traceless symmetric part of the square of the velocity gradient tensor
σ standard deviation
τ turbulent timescale
τ_{ij} subgrid-scale tensor
Ω_{ij} rate-of-rotational tensor
ω turbulence frequency

Subscripts and overlines
res resolved
SGS subgrid-scale
$\overline{()}$ filtered
$\widetilde{()}$ normalized by l and τ

the stagnation region for the round impinging jet. Chung et al. [13] used direct numerical simulation (DNS) to investigate the influence of the primary vortices on the unsteady heat transfer rate in the impinging flow of a planar impinging jet. The results showed that the primary vortices emanating from the nozzle have the main influence on the unsteadiness of the impinging heat transfer rate. Cziesla et al. [14] investigated the heat transfer and the unsteady flow in the stagnation region of a plane impinging jet with use of large-eddy simulation (LES) with the SGS model by Lilly [8], with satisfactory results.

A big issue in LES is to predict the near-wall behaviour where the subgrid-scale eddy-viscosity, ν_{SGS}, goes to zero at the wall with an asymptotic behaviour of $O(y^3)$. The Smagorinsky model, see Smagorinsky [15] gives a non-zero value at the wall due to non-zero velocity gradients and an asymptotic behaviour of $O(1)$. Additional modifications to the Smagorinsky model have been used to force the subgrid-scale eddy-viscosity to zero and to get correct asymptotic behaviour at the wall. Moin and Kim [16] used an exponential Van Driest damping function to account for the near-wall effects, see Van Driest [17]. A more suitable way to produce zero eddy-viscosity and correct asymptotic behaviour at the wall is to use the dynamic version of the Smagorinsky model by Germano et al. [18], where the Smagorinsky constant is determined in a dynamic procedure. The dynamic version of the Smagorinsky model is found to be unstable and averaging procedures or clipping are necessary to ensure stability. The averaging process is performed in the direction of statistical homogeneity for simpler cases, see Germano et al. [18] and Akselvoll and Moin [19]. Alternative approaches are needed for more complex flows where the direction of statistical homogeneity is difficult or impossible to determine. The localized dynamic model proposed by Ghosal et al. [20] and the Lagrangian dynamic model by Meneveau et al. [21] are two approaches to handle this problem. The SGS model by Nicoud and Ducros [22] yields correct asymptotic behaviour near the wall and the subgrid-scale eddy viscosity, ν_{SGS}, goes to zero without any *ad hoc* modifications or dynamic procedures. These qualities make the model well-suited for complex flows.

Two RANS-turbulence models, the $\overline{v^2}$-f model developed by Durbin [23] and a RSM with a two-layer model in the near-wall region, were used by Rundström and Moshfegh [24] in an earlier validation study of the turbulent flow from an impinging jet in a cross-flow on a wall-mounted cube. The models showed similar results near the walls and the RSM predicted the flow and turbulence characteristics better than the $\overline{v^2}$-f model in the free shear regions (i.e., far from the walls). The accuracy of the heat transfer prediction from the RSM was investigated by Rundström and Moshfegh [25] and the main features were well predicted by the model in all regions except in the stagnation region of the impinging jet, where the model seems to overpredict the heat transfer rate. This is an extension of the previous studies to investigate the performance of a LES with a SGS model by Nicoud and Ducros [22] on the turbulent flow and the heat transfer rate. The purpose of this study is to provide a thorough understanding of the physics in this complex flow and investigate the accuracy of the prediction of the mean velocity field, the turbulence characteristics and the heat transfer rate with use of a LES. The results from the LES are verified by infrared thermography and particle image velocimetry (PIV) measurements. The results are also compared with the RSM to evaluate the performance and to point out the strengths and weaknesses of this model.

2. Computational set-up and numerical scheme

2.1. Geometrical set-up and boundary conditions

The computational domain is a rectangular channel with a cube in the middle of the bottom wall (see Fig. 1). The channel has two inlets, one horizontal channel flow with a "low" velocity and one vertical impinging jet with a "high" velocity. The impinging jet enters through a circular nozzle in the middle of the top plate. The geometrical details and fluid properties are summarised in Tables 1 and 2.

The following boundary conditions are used: the top and bottom walls have no-slip conditions, symmetric boundary conditions are used for the sidewalls and zero-gradient condition for the outflow (i.e., $\partial u\partial t + u\partial u/\partial x = \partial T/\partial t + U\partial T/\partial x = 0$) with an overall mass balance correction. The same temperature, 20 °C, is used for the channel flow and the impinging jet. The mean velocity profile and the average values of the fluctuating velocity components at the inlet of the cross-flow (see Fig. 1) are predicted from a larger separate simulation with a row of wall-mounted cubes and the same geometrical configuration as in Fig. 1 under a fully-developed channel flow. The boundary conditions for the impinging jet, which are the mean velocity profile and the average values of the fluctuating velocity components, are derived from the measurements by Tummers et al. [26]. A curve fit from the velocity measurements is used to define the mean velocity profile, V. The average values of the fluctuating velocity components are assumed to be isotropic at the inlet of the impinging jet, i.e., $\overline{u'^2} = \overline{v'^2} = \overline{w'^2} = 2/3k$, and the turbulent kinetic energy, $k = 0.5(\overline{u'^2} + \overline{v'^2} + \overline{w'^2})$, is calculated by assuming that the streamwise and spanwise Reynolds stresses, $\overline{u'^2}$ and $\overline{w'^2}$, are identical. The values for $\overline{u'^2}$ and $\overline{v'^2}$ are obtained from the above mentioned measurements. It is worth mentioning that the mean velocities of cross-flow, U_c, and the impinging jet, U_j, are 1.73 and 6.50 m/s, respectively. Fig. 2 shows the boundary conditions used for the numerical simulation and the corresponding measured values at the centreline of the impinging jet. A spectral-based Random Flow Generation (RFG) technique is used to generate the instantaneous velocity profiles at the inlets. The original version of the RFG technique was proposed by Kraichnan [27] and later modified by Smirnov et al. [28], see Section 2.2.

The cube consists of an isothermal core of 70 °C, covered with an epoxy layer with low thermal conductivity and a thickness of 1.5 mm (see Fig. 1). The geometrical and material properties are summarised in Tables 1 and 2. The cooling medium is air.

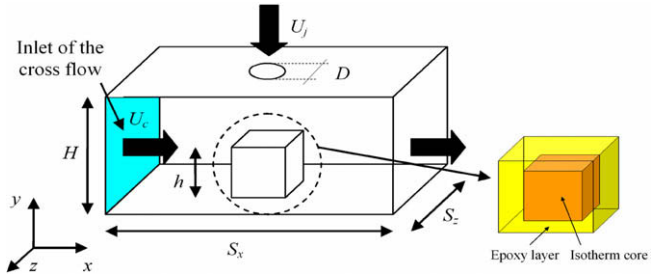

Fig. 1. Computational domain and a schematic sketch of the heated cube.

Table 1
Geometrical and flow details

D	12 mm
h	15 mm
H	$2h$ = 30 mm
S_x, S_z	$4h$ = 60 mm
$Re_j = U_jD/\nu$	5341
$Re_c = U_cH/\nu$	3554

Table 2
Material properties

	Air	Epoxy layer
Specific heat	1006.43	1668.5
Density	1.225	1150.0
Thermal conductivity	0.0242	0.236
Kinematic viscosity	1.46×10^{-5}	

2.2. Governing equations

The filtered three-dimensional incompressible continuity and Navier–Stokes equations are given by

$$\frac{\partial \bar{u}_i}{\partial x_i} = 0 \tag{1}$$

$$\frac{\partial \bar{u}_i}{\partial t} + \frac{\partial(\bar{u}_j\bar{u}_i)}{\partial x_j} = -\frac{1}{\rho}\frac{\partial \bar{p}}{\partial x_i} - \frac{\partial \tau_{ij}}{\partial x_j} + \nu\frac{\partial^2 \bar{u}_i}{\partial x_j \partial x_j} \tag{2}$$

$$\frac{\partial \overline{T}}{\partial t} + \frac{\partial(\bar{u}_i\overline{T})}{\partial x_i} = \frac{\partial}{\partial x_j}\left(\alpha\frac{\partial \overline{T}}{\partial x_j} - h_j\right) \tag{3}$$

where τ_{ij} and h_j are the modified subgrid-scale (SGS) tensor and the modified subgrid-scale heat fluxes. The SGS tensor, τ_{ij}, is given by

$$\tau_{ij} = \overline{u_iu_j} - \bar{u}_i\bar{u}_j \tag{4}$$

The SGS tensor with the eddy-viscosity hypothesis as

$$\tau_{ij} - \frac{1}{3}\delta_{ij}\tau_{kk} = 2\nu_{SGS}\bar{S}_{ij} \tag{5}$$

where $\bar{S}_{ij}$ is the resolved strain rate given by

$$\bar{S}_{ij} = \frac{1}{2}\left(\frac{\partial \bar{u}_i}{\partial x_j} + \frac{\partial \bar{u}_j}{\partial x_i}\right) \tag{6}$$

and where ν_{SGS} is the SGS eddy-viscosity. The WALE (wall-adapting local eddy viscosity) model by Nicoud and Ducros [22] was used to model the SGS eddy-viscosity as

$$\nu_{SGS} = L_s^2\frac{\left(\zeta_{ij}\zeta_{ij}\right)^{3/2}}{\left(\bar{S}_{ij}\bar{S}_{ij}\right)^{5/2} + \left(\zeta_{ij}\zeta_{ij}\right)^{5/4}} \tag{7}$$

where L_s is a length scale given by

$$L_s = \min\left(\kappa r,\ C_w V^{1/3}\right) \tag{8}$$

where κ is von Karman's constant, r is the normal distance to the closest wall, V is the volume of the computational cell and ζ_{ij} is the traceless symmetric part of the square of the velocity gradient tensor defined as

$$\zeta_{ij} = \frac{1}{2}\left(\frac{\partial \bar{u}_i}{\partial x_k}\frac{\partial \bar{u}_k}{\partial x_j} + \frac{\partial \bar{u}_j}{\partial x_k}\frac{\partial \bar{u}_k}{\partial x_i}\right) - \frac{1}{3}\delta_{ij}\frac{\partial \bar{u}_l}{\partial x_k}\frac{\partial \bar{u}_k}{\partial x_l} \tag{9}$$

The modified SGS heat fluxes, h_j, are defined as

$$h_j = \overline{u_jT} - \bar{u}_j\overline{T} \tag{10}$$

The modified SGS heat fluxes, h_j, are modelled by the eddy-diffusivity hypothesis with constant turbulent Prandtl number, Pr_t, as

$$h_j = -\frac{\nu_{SGS}}{Pr_t}\frac{\partial \overline{T}}{\partial x_j} \tag{11}$$

The following constants have been used in the LES model: $C_w = 0.325$, $\kappa = 0.4187$, $Pr_t = 0.85$.

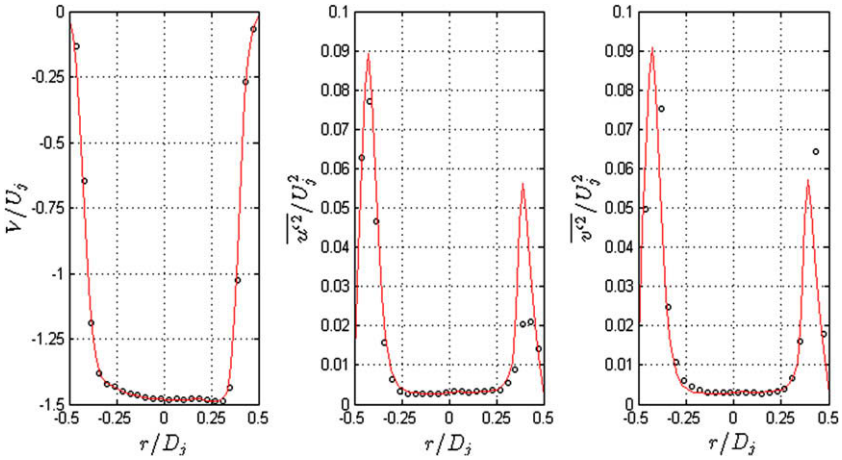

Fig. 2. Boundary conditions for the velocity profile, *V*, and the Reynolds stresses, used in the numerical simulation (solid line) and the corresponding measured values from the PIV measurement (circle symbol) at the centreline of the impinging jet.

The results from the LES are compared with results from a steady Reynolds stress model (RSM), where the pressure–strain term is modelled by a linear approach proposed by Launder and Shima [29]. The near-wall region was completely resolved all the way through the viscous sublayer by a two-layer approach. The two-layer model is based on the one-equation model of Wolfshtein [30] with use of the turbulent length scales proposed by Chen and Patel [31]. The turbulent heat fluxes are modelled by the eddy-diffusivity hypothesis with constant turbulent Prandtl number. Details about the modelling of the two-layer model can be found in the articles by Rundström and Moshfegh [24,25].

The spectral-based Random Flow Generation (RFG) algorithm by Smirnov et al. [28] was used to generate the instantaneous velocity field at the inlets. The steps to generate the instantaneous velocity components at the inlets are given by

$$a_{mi}a_{nj}\overline{u_iu_j} = \delta_{mn}c_{(n)}^2 \tag{12}$$

$$a_{ik}a_{kj} = \delta_{ij} \tag{13}$$

where $\overline{u_iu_j}$ is the Reynolds stresses, $c_n = [c_1, c_2, c_3]$, δ_{mn} is the Kronecker delta and a_{ij} is the orthogonal transformation tensor that diagonalizes $\overline{u_iu_j}$. Parentheses around indexes preclude summation. An unsteady velocity field is generated with the modified method by Kraichnan [27]:

$$v_i(x_j,t) = \sqrt{\frac{2}{N}}\sum_{n=1}^{N}\left[p_i^n\cos\left(\tilde{\kappa}_j^n\tilde{x}_j + \omega_n\tilde{t}\right) + q_i^n\sin\left(\tilde{\kappa}_j^n\tilde{x}_j + \omega_n\tilde{t}\right)\right] \tag{14}$$

$$\tilde{x}_j = \frac{x_j}{l}, \quad \tilde{t}_j = \frac{t}{\tau}, \quad \tilde{u} = \frac{l}{\tau}, \quad \tilde{\kappa}_j^n = \kappa_j^n\frac{\tilde{u}}{c_{(j)}} \tag{15–18}$$

$$p_i^n = \varepsilon_{ijm}\zeta_j^n\kappa_m^n, \quad q_i^n = \varepsilon_{ijm}\xi_j^n\kappa_m^n \tag{19 and 20}$$

$$\zeta_j^n, \xi_j^n, \omega_n \in N(0,1), \quad \kappa_j^n \in N(0,1/2)$$

where $l = k^{3/2}/\varepsilon$, $\tau = k/\varepsilon$ are turbulent length and time-scales, ε_{ijm} is the permutation tensor, $N(M,\sigma)$ is the normal distribution with mean M and standard deviation σ, and κ_j^n and ω_n represent a sample of n wave-number vectors and frequencies of the modelled turbulence spectrum

$$E(\kappa) = 16\left(\frac{2}{\pi}\right)^{1/2}\kappa^4\exp\left(-2\kappa^2\right) \tag{21}$$

The flow field, v_i, generated in the previous time step is scaled and orthogonally transformed to obtain a new flow field, u_i, by

$$w_i = c_{(i)}v_{(i)} \tag{22}$$

$$u_i = a_{ij}w_j \tag{23}$$

2.3. Numerical details

The finite-volume code Fluent 6.2.16 was used to numerically solve the governing equations with a segregated scheme and the PISO (pressure implicit with splitting of operators) algorithm by Issa [32] solved the pressure–velocity coupling. The spatial discretization consisted of a bounded central-differencing scheme by Leonard [33] for the nonlinear terms and the second-order central scheme for the viscous terms. The time integration was performed by a second-order implicit scheme. The time step, Δt, was set to 5.3115×10^{-5} s and kept constant during the simulation. The estimated time step provides the CFL numbers to be lower than 0.6 in the whole computational domain with exception for the regions near the edges on the top of the cube where a maximum value close to 1.4 has been observed. The sampling time for the time statistics is 0.5040 s (or 9488 time steps). No significant change was observed for the samplings variables after 0.307 s which indicates that the length of the sampling time is enough. The numerical details are summarized in Table 3.

For an accurate LES predictions the resolution of the grid must be fine enough to resolve all the large energy-containing eddies and the modelling of the small-scaled eddies should not take place before the inertial subrange. As a presentation of the grid quality one need to keep the ratio between SGS eddy-viscosity and molecular viscosity, ν_{SGS}/ν, below 0.5. Fig. 3 shows the ratio between SGS eddy-viscosity and molecular viscosity, ν_{SGS}/ν, as a function of the

Table 3
Numerical scheme

Grid	Staggered grid
Pressure–velocity coupling algorithm	PISO
Spatial discretization	
Nonlinear terms	Bounded central scheme
Viscous terms	Second-order central scheme
Time advancement	
Time discretization	Second-order implicit scheme
Time step size, Δt	5.3115×10^{-6} s
Sampling time	0.5040 s

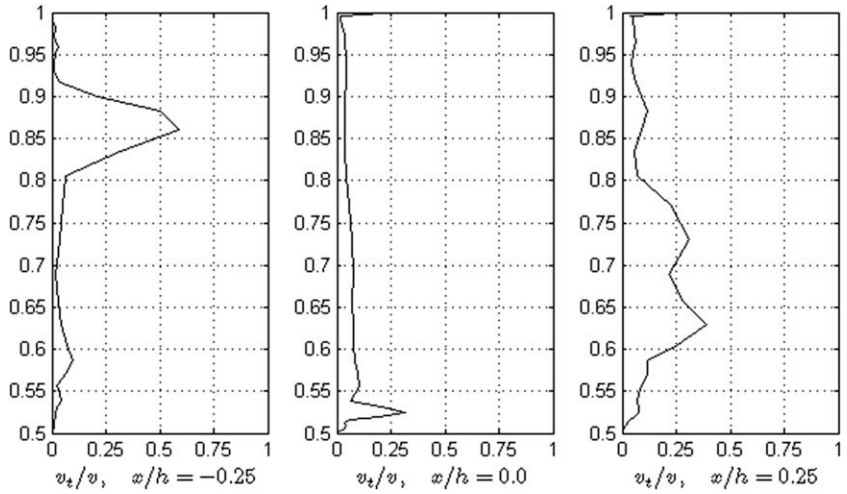

Fig. 3. SGS eddy-viscosity, v_{SGS}, in the xy-plane, $z/h = 0$ at time 0.307 s.

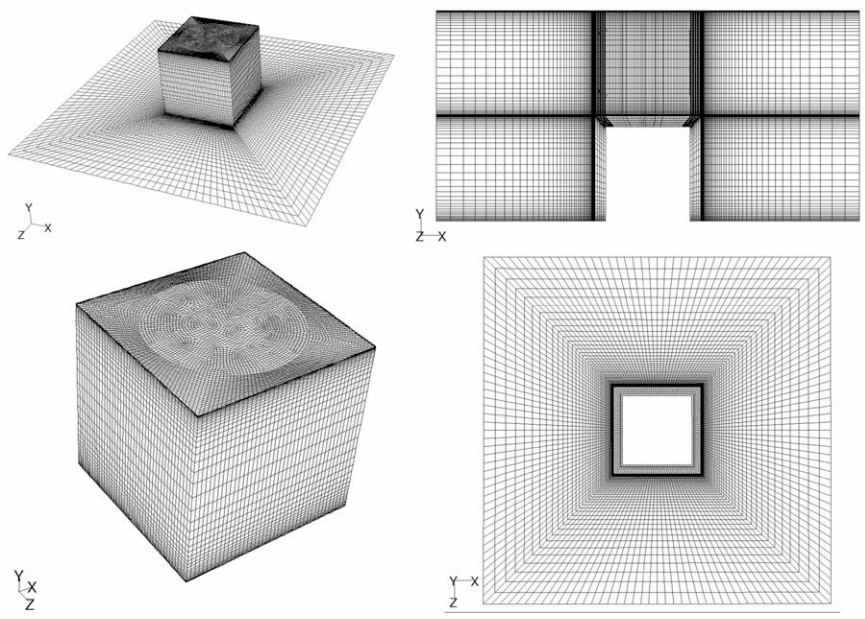

Fig. 4. Computational grid, perspective view (upper left), side view (upper right), cube surface (lower left), top view (lower right).

vertical distance (y/H) above the third cube. Each diagram represents different locations in the x-direction at the centre of the cube. The first diagram represents the line at the distance $0.25h$ downstream from the centre of the cube (i.e., $x/h = -0.25$), and the following diagrams represent the following x-positions: $x/h = 0.0$, and $x/h = 0.25$, which corresponds the centreline and the shear regions of the impinging jet. As it is shown in Fig. 3 the values of v_{SGS}/v, are lower than or close to 0.5 in all three diagrams. This corresponds to a maximum value of a ratio between the modelled and resolved turbulent kinetic energy, k_{SGS}/k_{res}, lower than 4×10^{-3}, where k_{SGS} is estimated by $k_{SGS} = (v_{SGS}/L_s)^2$. This indicates that the cut-off wave-number is in the inertial subrange in these regions.

Based on the above constraint the computational grid consists of 881,832 structured hexahedral cells was generated. There are 42×42 cells near the sidewalls of the cube. The top of the cube consists of a total of 5876 cells. The circular inlet and the region under the impinging jet consist of 2516 cells in the xz-plane. The mesh is refined enough near the solid walls ($y^+ < 0.6$) to resolve the all-boundary layers with more than 4 nodes in the region $y^+ = 0$–5 and with more than 10 nodes in the region $y^+ = 0$–30, see Fig. 4. There are five cells with identical spacing through the epoxy layer and there are 64,660 cells located in the epoxy layer.

3. Experimental details

3.1. Experimental set-up

The experimental set-up is shown in Fig. 5. The experimental equipment consists of a wind tunnel with five cubes mounted in line in the middle of the tunnel; only the third is heated in the present study. The size of the cubes is 15 mm and the distance between each pair of cubes S_x is 60 mm. The tunnel has a height H of 30 mm and a width of 360 mm. One impinging jet is positioned above the third cube. The impinging jet is forced through a circular hole with a diameter, D, of 12 mm. The centres of the impinging jets and the third cube are identical. The impinging jet is provided with air from a separate channel placed above the top plate. The

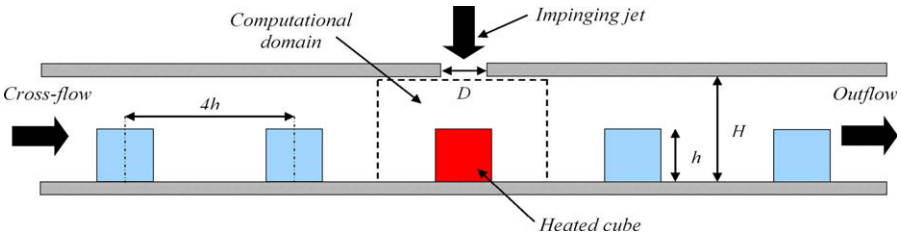

Fig. 5. Schematic sketch of the experimental set-up.

inlet air temperature has been kept constant at 20 °C during the measurement. All measurements are carried out at the third cube (see Fig. 5).

3.2. Measurements

The time-average velocity field and the Reynolds components were measured in the *xy* and *xz* planes with a particle image velocimetry (PIV) system. The PIV system included a double-pulsed Nd:YAG laser with a pulse energy of 25 mJ. The laser was used to produce an approximately 1 mm light sheet that illuminated the seed particles in the flow. A PCO Sensicam camera recorded the images of the seed particles in the light sheet. For each plane, 1000 image pairs were acquired and the commercial software VidPIV Rowan v4.0 was used to analyse the images.

The time-averaged temperature distribution on the cube was measured by a low-wavelength (2–5.5 μm) infrared imaging system (Varioscan, Jenoptik). The Varioscan camera is equipped with a scanning mechanism to create images that are composed at 200 lines with 300 pixels. The relation between the pixel intensity and the temperature is established in an in-situ calibration procedure in conjunction with an image restoration technique based on a Wiener filter, using the two-dimensional optical transfer function as described by Meinders et al. [34]. These temperature and PIV measurements were carried out at the Department of Applied Physics, Delft University of Technology, Delft, the Netherlands, see Tummers et al. [26] for more details.

4. Computational results

Isosurfaces of the second invariant of the velocity gradient tensor q defined as

$$q = -\frac{1}{2}\frac{\partial \bar{u}_i}{\partial x_j}\frac{\partial \bar{u}_j}{\partial x_i} = \bar{S}_{ij}\bar{S}_{ij} - \bar{\Omega}_{ij}\bar{\Omega}_{ij} \tag{24}$$

were used to visualise the complex turbulent structures around the cube. Fig. 6 shows the instantaneous isosurface of q coloured by velocity magnitude. Fig. 6 describes both the larger turbulent structures ($q = 6 \times 10^4$) and the smaller turbulent structures ($q = \pm 10^7$). The larger scales are observed along the sidewalls, behind the rear side and around the lower part of the cube. The smaller structures are observed in the free shear regions between the impinging jet and the cross-flow and at the separations from the top of the cube. Long vortexes parallel with the sidewall are created from the separation at the edge between the front and the sidewalls of the cube. These vortexes move along the sidewalls to the separation at the edge between the sidewalls and the rear side of the cube. The smaller turbulent structures ($q = \pm 10^7$) in the region between the impinging jet and the cross-flow are concentrated to a radial distance of approximately the nozzle radius.

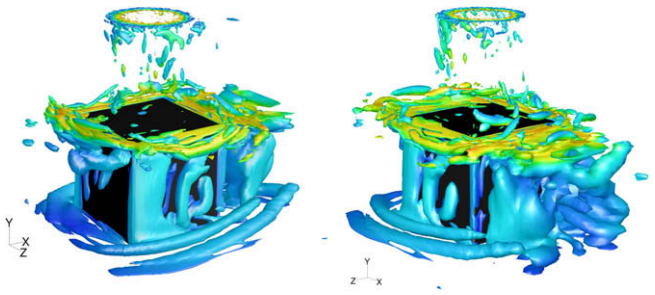

Fig. 6. Instantaneous isosurface of q at time 0.307 s, coloured by velocity magnitude (colour scale 0–12), $q = 10^7$ and 6×10^4, front-side view (left), rear-side view (right).

Fig. 7 shows the instantaneous isosurface of temperature, T, at the time 0.307 s. The image is coloured by the velocity magnitude. Several similarities between the turbulent velocity and temperature field near the cube can be observed from Figs. 6 and 7. The turbulent vortex structures near the cube have a significant influence on the temperature field, where the large-scale vortices are impor-

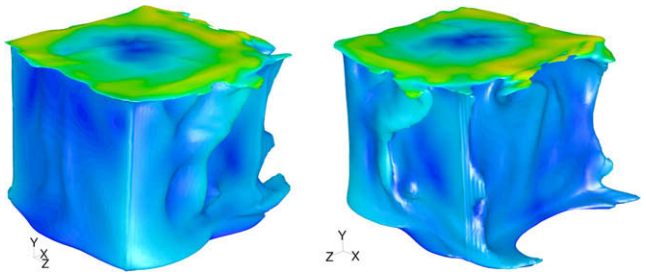

Fig. 7. Instantaneous isosurface of temperature, T, at time 0.307 s, coloured by velocity magnitude (colour scale 0–12), $T - T_\infty = 9$ °C, front-side view (left), rear-side view (right).

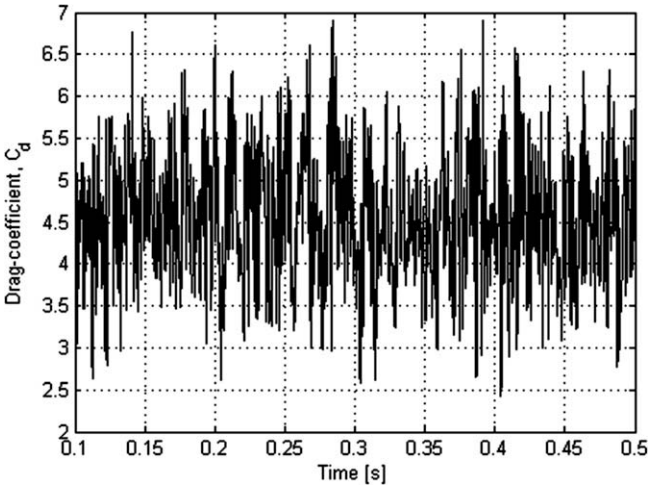

Fig. 8. Time history of the drag-coefficient, C_d, in the x-direction.

tant in the turbulent heat transport mechanisms. The turbulent vortex structures at the separations from the edges carried a large amount of heat (see Fig. 7).

The time history of the drag-coefficient, C_d, in the x-direction (see Fig. 8) is used to illustrate the unsteadiness. The average frequency is 609.2 s^{-1}, which corresponds to 307 cycles during the total sampling time. The average value and the RMS-value of the drag-coefficient, C_d, are 4.54 and 0.610, respectively.

Fig. 9 shows the normalized y-velocity component (V/U_j), $\overline{u'^2}$ Reynolds stress and $\overline{v'^2}$ Reynolds stress in the centre of the impinging jet as a function of the normalized vertical distance y/H. The resolved Reynolds stresses from the LES are presented in Fig. 9 and later in this article.

The left diagram in Fig. 9 shows that the y-velocity component is almost constant when 0.85 (y/H, an exponentially decreasing behaviour is observed between $0.85 \leqslant y/H \leqslant 0.55$ and a linearly decreasing behaviour when $y/H \leqslant 0.55$. The agreement between the PIV measurements and the simulations are good. The only deviation from the PIV measurements is in the exponential region, where the results from the simulations show somewhat lower values.

The middle diagram in Fig. 9 shows that the increase of $\overline{u'^2}$ Reynolds stress with increasing y-coordinates near the wall (i.e., when $y/H = 0.5$) is identical for both the RSM and the LES but the maximum value is significant lower and located at a lower position in the LES than in the RSM. The $\overline{u'^2}$ Reynolds stress is almost constant from the outlet of the nozzle down to the distance of $y/H \leqslant 0.55$ where a rapid increase in $\overline{u'^2}$ Reynolds stress occurs in both predictions. The LES shows a lower level of $\overline{u'^2}$ Reynolds stress than the RSM and the PIV measurements in this region.

The right diagram in Fig. 9 shows that the RSM predicts a much higher level of $\overline{v'^2}$ Reynolds stress in the stagnation region than the LES and the PIV measurements do. The increase of $\overline{v'^2}$ Reynolds stress with increasing y-coordinates is much faster in the RSM near the wall (i.e., when $y/H = 0.5$) than in the LES and the PIV measurements, and the maximum value is more than seven times larger in the RSM than in the LES and the RSM predicts the level of $\overline{v'^2}$ Reynolds stress is more than three times higher than the level of $\overline{u'^2}$ Reynolds stress in the stagnation region. The generation of $\overline{v'^2}$ Reynolds stress occurs in two terms in the transport equations for the Reynolds stresses, in the production term, $P_{22} = -\overline{v'^2}\partial V/\partial y$, and in the pressure–strain term, Φ_{22}. The production term, P_{22}, is obtained directly from the governing equations while the pressure–strain term, $\Phi_{22} = \overline{2(p'/\rho)\partial v'/\partial y}$, has been modelled in order to close the system of equations which indicates that a modification of the pressure–strain term is necessary to improve the results from the RSM. This is a well-known phenomenon for impinging flows when the modelling of the wall-reflection term in the pressure–strain term is based on the model by Gibson and Launder [35]. Craft et al. [6] observed similar results when this pressure–strain model was used for two cases with axisymmetric round jets impinging normally on a flat surface. The results have been improved significantly by simulating the cases with a new modified

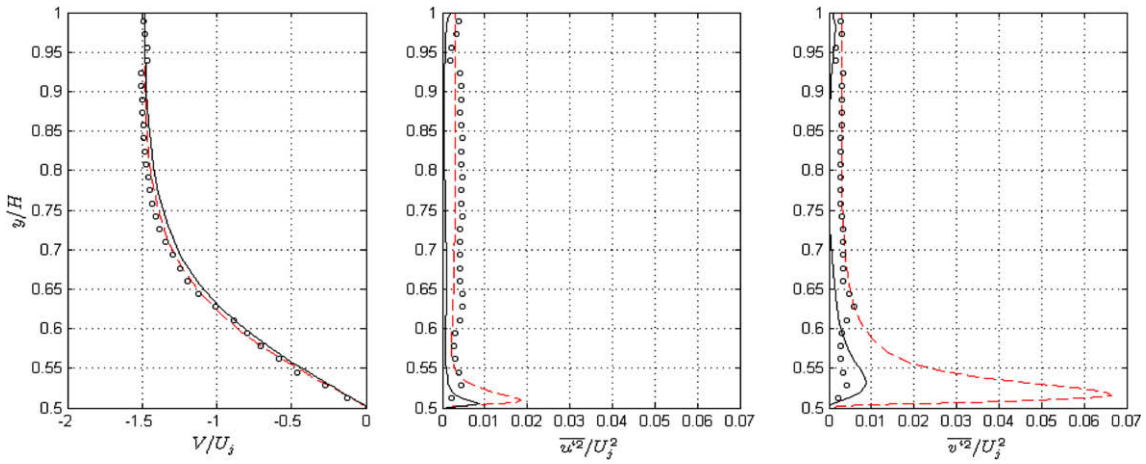

Fig. 9. y-velocity components (V/U_j), $\overline{u'^2}$ Reynolds stress and $\overline{v'^2}$ Reynolds stress in the y-direction at $x/h = z/h = 0$. - - -, RSM; —, LES; o, and PIV measurement.

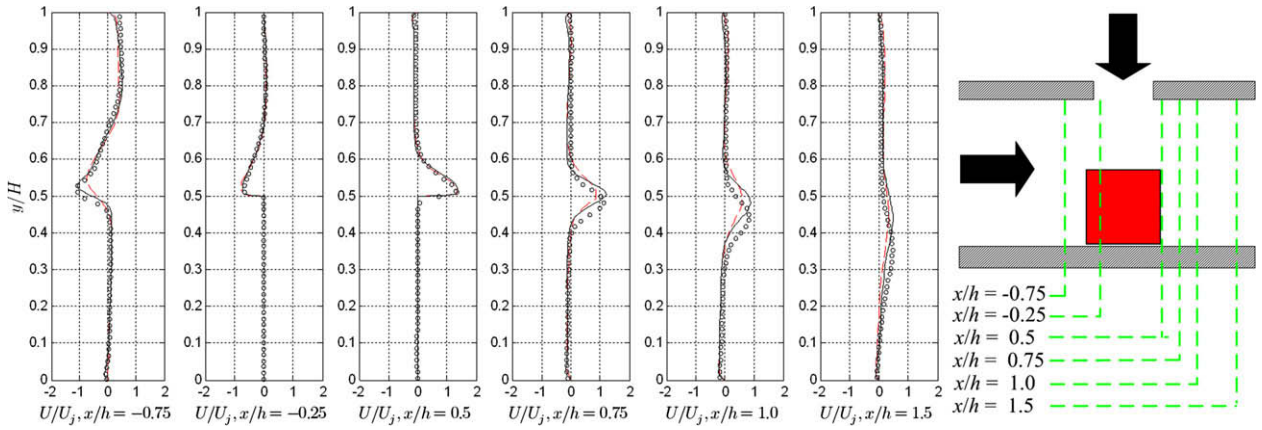

Fig. 10. x-velocity components (U/U_j) in the xy-plane, $z/h = 0$. - - -, RSM; —, LES; and o, PIV measurement.

wall-reflection terms in the pressure–strain term, see Craft et al. [6].

Fig. 10 shows the normalized x-velocity component (U/U_j) as a function of the vertical distance (y/H) near the third cube. Each diagram represents different locations in the x-direction at the centre of the cube. The first diagram represents the line at the distance $0.75h$ upstream from the centre of the cube (i.e., $x/h = -0.75$), and the four following diagrams represent the following x-positions: $x/h = -0.25$, $x/h = 0.5$, $x/h = 0.75$, $x/h = 1$ and $x/h = 1.5$ where the last four x-positions represent the distance downstream from the centre of the cube.

The second and third diagrams in Fig. 10 show good agreement between the RSM, LES and the PIV measurement in the stagnation region. Both models show good agreement with the PIV measurement in the recirculating region before the front side of the cube (see the first diagram on the left in Fig. 10). Both models and the PIV measurement show almost identical behaviour at the upper part of the recirculating region ($0.7 \leqslant y/H \leqslant 0.9$) at $x/h = -0.75$. The LES agrees well with the PIV measurement at the lower part of the recirculating region ($0.5 \leqslant y/H \leqslant 0.55$) at $x/h = -0.75$, where the RSM shows somewhat lower values (see the first diagram in Fig. 10). The strong separation from the rear side is also well predicted by the models (see the third diagram from the left in Fig. 10) but the separated flow seems to be more forced against the bottom plate in the PIV measurement, which results in a lower position of the maximum value in the PIV measurement than in the RSM and in the LES (see the fourth and fifth diagrams from the left in Fig. 10). The predicted peak from the RSM seems to decrease faster than the peaks in the LES and in the PIV measurement (see the fourth and fifth diagrams from the left in Fig. 10).

Fig. 11 shows the normalized $\overline{u'^2}$ Reynolds stress as a function of the vertical distance (y/H) at the centre-line near the third cube. The representation of each diagram is identical with Fig. 10.

The predicted $\overline{u'^2}$ Reynolds stresses are in good agreement with the PIV measurement in the stagnation region, where the maximum values of the peaks are almost identical between the RSM and the PIV measurement (see the second and third diagrams in Fig. 11). The LES shows a somewhat lower value of the maximum at $x/h = -0.25$ than the RSM and the PIV measurement. Two peaks are observed in the region before the front side of the cube in both simulations and in the PIV measurements. These peaks can be explained by the recirculation vortex. The results from the RSM show a higher value of the lower peak than the LES and the PIV measurement (see the first diagram in Fig. 11). The predicted $\overline{u'^2}$ Reynolds stresses from both models are almost identical with the PIV measurement when the separation leaves the rear side of the cube (see the third diagram from the left in Fig. 11). The maximum value of the peak is somewhat higher in the RSM than in the LES and in the PIV measurement at $x/h = 0.75$ (see the fourth diagram in Fig. 11). This indicates that the net production of $\overline{u'^2}$ Reynolds stresses is higher in the RSM than in the LES and in the PIV measurement in this region. The deviations of the maximum values are smaller at $x/h = 1.0$ and the LES shows a somewhat lower value than the RSM and the PIV measurement (see the fifth diagram in Fig. 11). The RSM and the LES predicts the vertical positions of

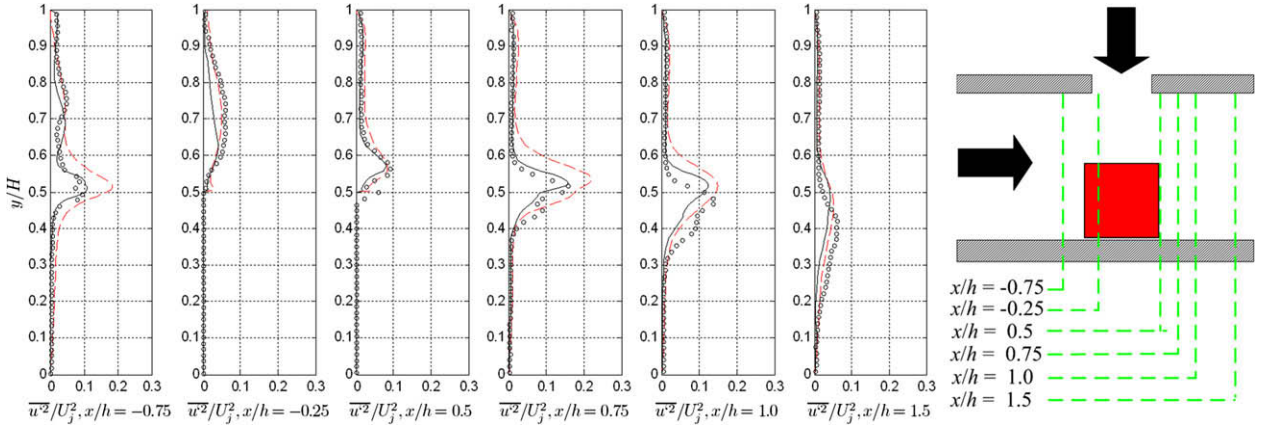

Fig. 11. $\overline{u'^2}$ Reynolds stress in the xy-plane, $z/h = 0$. - - -, RSM; —, LES; and o, PIV measurement.

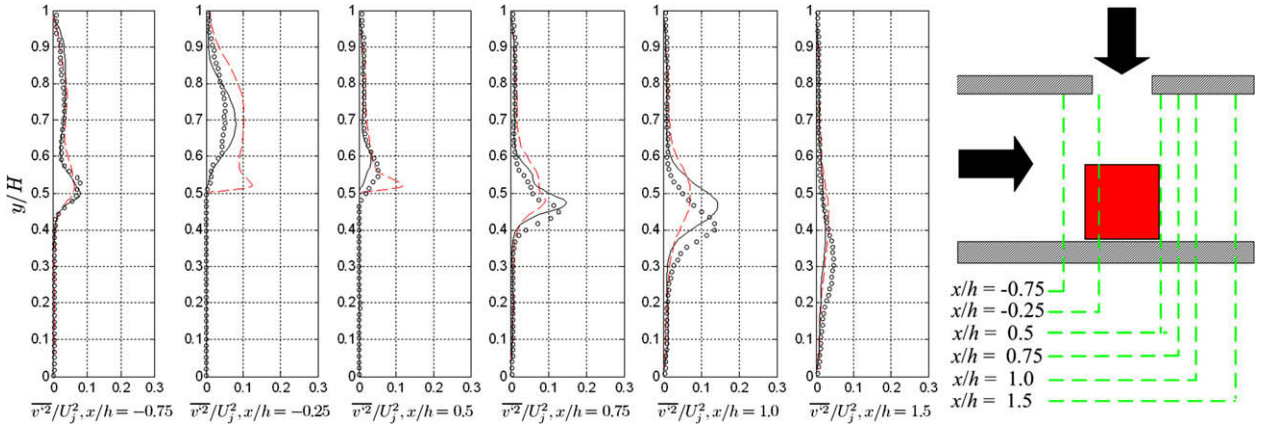

Fig. 12. $\overline{v'^2}$ Reynolds stress in the xy-plane, $z/h = 0$. - - -, RSM; —, LES; and o, PIV measurement.

the maximum in higher regions than the PIV measurement at $x/h = 1$ (see the fifth diagram in Fig. 11).

Fig. 12 shows the normalized $\overline{v'^2}$ Reynolds stress as a function of the vertical distance (y/H) in the centreline near the third cube. The representation of each diagram is identical with Fig. 10.

Fig. 12 shows that a significant peak is observed in the stagnation region in the predicted $\overline{v'^2}$ Reynolds stress from the RSM at a distance located at approximately $y/H = 0.52$ (see the second diagram in Fig. 12). This peak is not observed in the LES or in the PIV measurement. Two similar peaks are observed at $x/h = -0.75$ (see the first diagram in Fig. 12) in the simulations and in the PIV measurement. This higher net production of $\overline{v'^2}$ Reynolds stresses in the stagnation region results in a significantly higher maximum level of $\overline{v'^2}$ Reynolds stress in the RSM at the separation from the rear part of the top of the cube (see the third diagram in Fig. 12). The maximum value of $\overline{v'^2}$ Reynolds stress decreases faster in the RSM than in the LES and in the PIV measurement in the region behind the rear side. The maximum is located in a lower region in the PIV measurement than in the RSM and the LES (see the fourth and fifth diagrams in Fig. 12).

Fig 13 shows the normalized $\overline{u'v'}$ Reynolds stress as a function of the vertical distance (y/H) in centreline near the third cube. The representation of each diagram is identical with Fig. 10.

Two significant peaks can be observed in the $\overline{u'v'}$ Reynolds stress in the shear region from the separations of the cube. The agreement between the LES and the PIV measurement are better than between the RSM and the PIV measurement at the front side of the cube especially for the upper negative peak (see the first diagram in Fig. 13). The same trend is observed above the rear side of the cube: the agreement is better between the LES and the PIV measurement than between the RSM and the PIV measurement (see the third diagram in Fig. 13). The upper (positive) peak increases more in the LES then the RSM and in the PIV measurements between $x/h = 0.5$ and $x/h = 0.75$ (see the third and fourth diagram in Fig. 13). Both peaks decrease in the predictions with approximately the same rate between $x/h = 0.75$ and $x/h = 1.0$. The values for the upper peaks are quite equal to each other, while the prediction of the magnitude of the lower peaks are somewhat lower in both simulations than in the PIV measurement at $x/h = 1.0$ (see the fifth diagram in Fig. 13). The positions are located at a higher distance from the bottom plate in the RSM and in the LES than in the PIV measurement (see the fourth and fifth diagrams in Fig. 13) which again indicates that the measured separation from the top of the cube forces more against the bottom plate in the PIV measurement than in the RSM and in the LES.

Fig. 14 shows the normalized x-velocity component (U/U_j) as a function of the spanwise distance (z/h) at the vertical location of 4 mm (or $y/H = 2/15$). Each diagram represents the same x-positions as in Fig. 10.

The blockage effect in front of the front side of the cube predicted by the RSM and the LES is in very good agreement with the PIV measurement (see the first diagram in Fig. 14). The bypass flow is in good agreement between the RSM, the LES and the PIV measurement and the predictions of the separated flows from the sidewalls are also in good agreement with the PIV measurement (see the second and third diagrams in Fig. 14). The agreement between the predictions and the PIV measurement in the wake region behind the rear side is better close to the rear side than farther

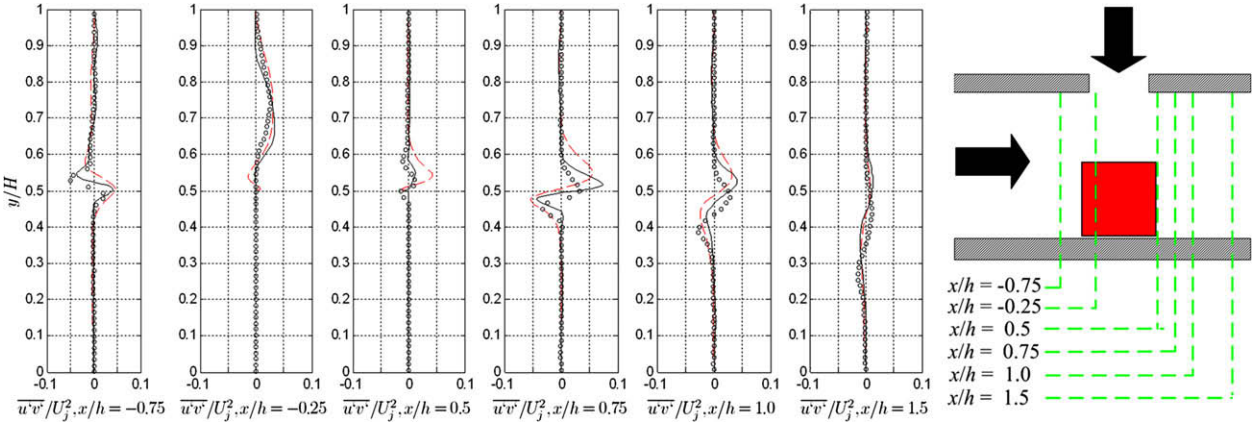

Fig. 13. $\overline{u'v'}$ Reynolds stress in the xy-plane, $z/h = 0$. - - -, RSM; —, LES; and o, PIV measurement.

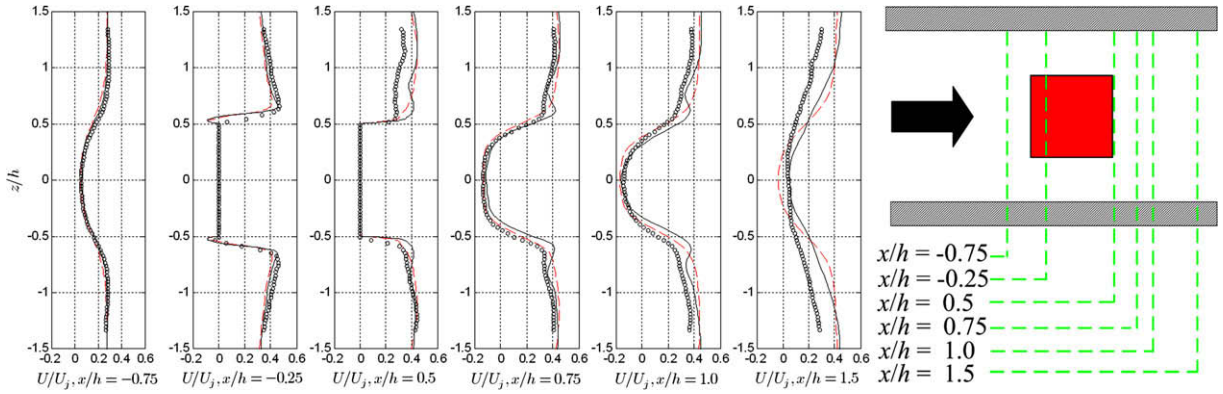

Fig. 14. x-velocity components (U/U_j) in the xz-plane, $y/h = 4/15$. - - -, RSM; —, LES; and o, PIV measurement.

downstream from the wall, and the agreement is better near the centreline ($-0.5 \leqslant z/h \leqslant 0.5$) than in the periphery (see the fourth, fifth and sixth diagrams in Fig. 14). A local maximum can be observed in the LES at $z/h \approx \pm 0.6$ and this maximum is not observed in the RSM or in the PIV measurements (see the fourth and fifth diagrams in Fig. 14). Agreement is very good between LES and in the PIV measurement near the centreline in the wake flow; the length of the wake seems to be a little bit larger in the RSM than in the LES and in the PIV measurement (see the sixth diagram in Fig. 14). Both simulations show less diffusivity in the wake region than the PIV measurement and the RSM shows somewhat lower diffusivity than the LES in this region (see the sixth diagram in Fig. 14).

The contour plots in Fig. 15 and the diagrams in Fig. 16 show the temperature distribution along two path lines on the surface of the cube. Both models show good agreements with the measurement on the front side of the cube and the results from LES are somewhat closer to the measured values. The rapidly decreasing temperatures near the edges are also well predicted by both simulations. The heat transfer rate in the stagnation region at the top of the cube seems to be a bit overpredicted by the RSM, due to the lower temperature on the top of the cube. The results from the LES agree much better with the measurement at the top of the cube. The opposite trend is observed on the rear side of the cube, where the predicted temperature from the RSM is higher than the measured and the results from the LES are somewhat higher than the measured. The positions of the maximum values in the vertical direction on the rear side of the cube are well predicted by both simulations (see the left diagram in Fig. 16), despite the fact that the temperatures seem to be more or less overpredicted. The rapidly decreasing temperature in the measurement near the bottom plate can be explained by the heat losses through the base plate at the bottom of the cube (see the left diagram in Fig. 16). The predicted temperatures show an increasing trend near the bottom plate due to the adiabatic boundary condition on the bottom plate. The predicted temperature agrees well with the measurement on the sidewall of the cube (see the right diagram in Fig. 16). A maximum value is observed in both simulations and in the measurement near the front side on the sidewall where the recirculating occurs, a minimum is observed at the middle of the sidewall at the reattachment points (see the right diagram in Fig. 16). The predicted heat transfer rate from the RSM in the stagnation region on the top of the cube can be decreased by adding the Yap correction as an extra source term in the transport equation for the turbulent

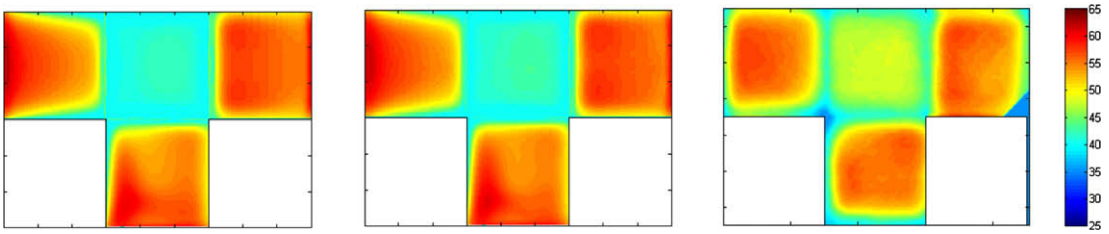

Fig. 15. Contours of surface temperature, RSM (left), LES (middle), measurement (right).

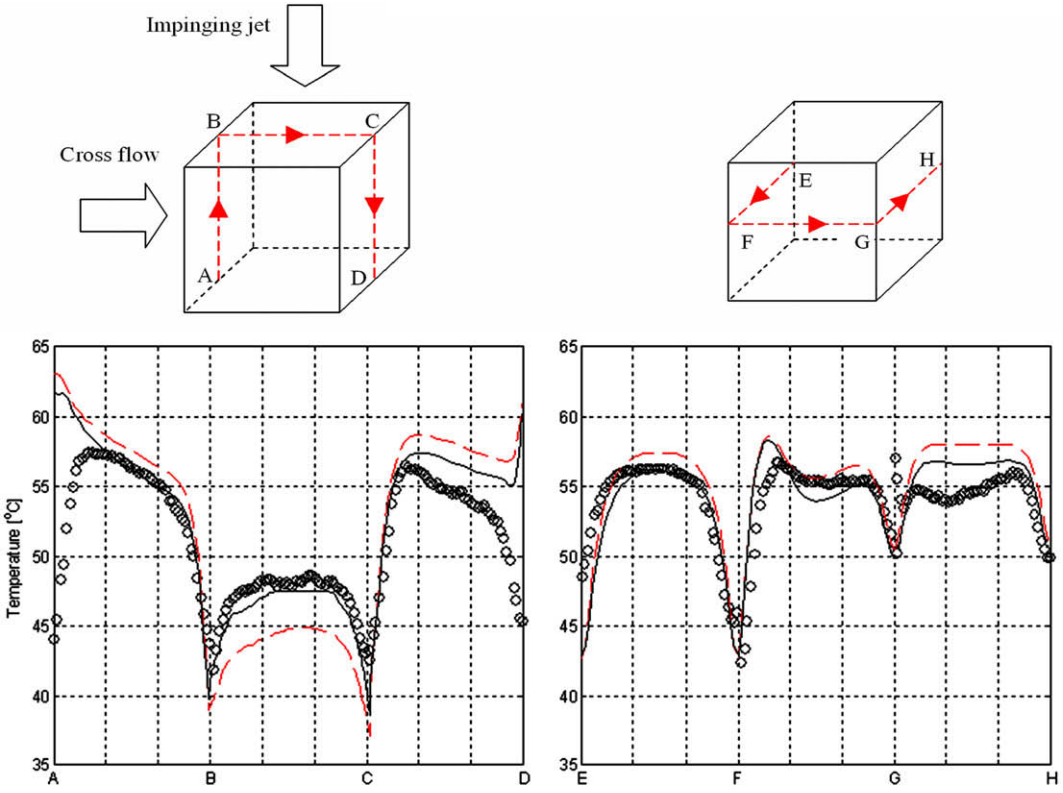

Fig. 16. Surface temperature, in the *xy*-plane, $z/h = 0$ (left), in the *xz*-plane, $y/h = 0.5$ (right), - - -, RSM; —, LES; and *o*, measurement.

dissipation rate, ε, which decrease the turbulent length scales, $l=k^{3/2}/\varepsilon$, and the turbulent heat transfer rate. It is also necessary to modify the turbulent length scales in the two-layer model near the wall due an extensive part of the temperature drop occurs in this region.

5. Conclusions and discussion

The investigation has shown that the RSM and the LES predict the mean velocity, turbulence characteristics and temperature for an impinging jet in the cross-flow on a heated wall-mounted cube with good agreement with measurements. The results revealed that the flow structure is highly complex and the there are several flow-related phenomena, such as stagnation points, separations, recirculating and curvature effects which have to be predicted. Both simulations predict the mean velocity field well in the stagnation region and in the other near-wall regions. The RSM seems to predict the Reynolds stresses well in all regions except for the stagnation region above the cube, where the $\overline{v'^2}$ Reynolds stresses are much higher than in the LES and in the PIV measurement and seem to be overpredicted in the RSM. This deviation can be traced to the near-wall handling pressure–strain term in the transport equations for the Reynolds stresses. Both temperature predictions capture the main features on all five walls from the measurement. The temperature prediction from the LES is in much better agreement with the measurement than the RSM at the stagnation region on the top of the cube where the RSM seems to overpredict the heat transfer rate. A possible method to solve this problem is to add the Yap correlation as an extra source term to the transport equation for the dissipation rate of turbulence, ε, which decrease the length scales, $l = k^{3/2}/\varepsilon$, and the turbulent heat transfer rate in the stagnation region. The length scales The temperature prediction from the LES is also more close to the measurement than the RSM on the front and rear side of the cube. The random flow generation (RFG) used at the inlets in the LES generates significantly lower levels of the fluctuating velocity components than in the PIV measurement. The heat transfer coefficient in the stagnation region on the top of the cube is very sensitive to the boundary condition at the inlet of the impinging jet, see e.g., Behnia et al. [4], and a higher level of the fluctuating velocity components should result in higher heat transfer coefficients and lower surface temperatures on the top of the cube.

Acknowledgements

The authors gratefully acknowledge the funding received from the KK Foundations, Ericsson AB, Nokia AB and University of Gävle. The authors thank Dr. M. Tummers and Professor K. Hanjalić at Delft University of Technology, The Netherlands, for their contribution in the experimental part of this project.

References

[1] E.R. Meinders, Experimental Study of Heat Transfer in Turbulent Flows Over Wall-mounted Cubes, Ph.D. Thesis, Delft University of Technology, The Netherlands, 1998.
[2] D. Rundström, B. Moshfegh, Investigation of flow and heat transfer of an impinging jet in a cross-flow for cooling of a heated cube, ASME J. Electron. Pack. 128 (2006) 150–156.
[3] J. Lee, S.J. Lee, Stagnation region heat transfer of a turbulent axisymmetric jet impingement, Exp. Heat Transfer 12 (1999) 137–156.
[4] M. Behnia, S. Parniex, P. Durbin, Numerical study of turbulent heat transfer in confined and unconfined impinging jets, Int. J. Heat Fluid Flow 20 (1998) 1–9.
[5] A. Abdon, B. Sundén, Numerical investigation of impingement heat transfer using linear and nonlinear two-equation turbulence models, Numer. Heat Transfer A 40 (2001) 563–578.
[6] T.J. Craft, L.J.W. Graham, B.E. Launder, Impinging jet studies for turbulence models. Assessment II: An examination of the performance of four turbulence models, Int. J. Heat Mass Transfer 36 (1993) 2685–2697.
[7] F. Beaubert, S. Viazzo, Large eddy simulations of plane turbulent impinging jets at moderate Reynolds numbers, Int. J. Heat Fluid Flow 24 (2003) 512–519.
[8] D. Lilly, A proposed modification of the Germano subgrid-scale closure method, Phys. Fluids A 4 (1992) 633–635.
[9] S. Maurel, C. Solliec, The plane air jet impinging nearby and far from flat plate, Exp. Fluids 31 (2001) 687–697.
[10] M. Olsson, L. Fuchs, Large eddy simulation of a semiconfined circular impinging jet, Phys. Fluids 10 (1998) 476–486.
[11] S. Liu, C. Meneveau, J. Katz, On the properties of similarity subgrid-scale models as deduced from measurements in a turbulent jet, J. Fluid Mech. 275 (1994) 83–119.
[12] M. Tsubokura, T. Kobayashi, N. Taniguchi, W.P. Jones, A numerical study on the eddy structures of impinging jets excited at the inlet, Int. J. Heat Fluid Flow 24 (2003) 500–511.
[13] Y.M. Chung, K.H. Luo, N.D. Sandham, Numerical study of momentum and heat transfer in unsteady impinging jets, Int. J. Heat Fluid Flow 23 (2002) 592–600.
[14] T. Cziesla, G. Biswas, H. Chattopadhyay, N.K. Mitra, Large-eddy simulation of flow and heat transfer in an impinging slot jet, Int. J. Heat Fluid Flow 22 (2001) 500–508.
[15] J. Smagorinsky, General circulation experiments with the primitive equations. I. The basic equations, Mon. Weather Rev. 91 (1963) 99–164.
[16] P. Moin, J. Kim, Numerical investigation of turbulent channel flow, J. Fluid Mech. 118 (1982) 341–377.
[17] E.R. van Driest, On turbulent flow near a wall, J. Aeronaut. Sci. 23 (1956) 1007–1011.
[18] M. Germano, U. Pomelli, P. Moin, A. Cabot, Dynamic subgrid-scale eddy viscosity model, Phys. Fluids A 3 (1991) 1760–1765.
[19] K. Akselvoll, P. Moin, Large-eddy simulation of turbulent confined coannular jets, J. Fluid Mech. 315 (1996) 387–411.
[20] S. Ghosal, T.S. Lund, P. Moin, K. Akselvoll, A dynamic localization model for large-eddy simulation of turbulent flows, J. Fluid Mech. 286 (1995) 229–255.
[21] C. Meneveau, T. Lund, W. Cabot, A Lagrangian dynamic subgrid-scale model of turbulence, J. Fluid Mech. 319 (1996) 353–385.
[22] F. Nicoud, F. Ducros, Subgrid-scale stress modelling based on the square of the velocity gradient tensor, Flow Turbul. Combust. 62 (1999) 183–200.
[23] P. Durbin, Near-wall turbulence closure modelling without damping function, Theor. Computat. Fluid Dyn. 3 (1991) 1–13.
[24] D. Rundström, B. Moshfegh, RSM and $\overline{v^2}$-f study on the flow behaviour of an impinging jet in a cross-flow on a wall-mounted cube, Prog. Computat. Fluid Dyn. 7 (2007) 311–322.
[25] D. Rundström, B. Moshfegh, RSM predictions of an impinging jet in a cross flow on a wall-mounted cube, in: Proceedings of the 13th International Heat Transfer Conference, 13–18 August, 2006, Sydney, Australia, 2006.
[26] M.J. Tummers, M.A. Flikweert, K. Hanjalić, R. Rodink, B. Moshfegh, Impinging jet cooling of wall-mounted cubes, in: Proceedings of the ERCOFTAC International Symposium on Engineering Turbulence Modelling and Experiments – ETMM6, Sardinia, Italy, 2005, pp. 773–782.
[27] R. Kraichnan, Diffusion by random velocity field, Phys. Fluids 13 (1970) 22–31.
[28] A. Smirnov, S. Shi, I. Celik, Random flow generation technique for large eddy simulations and particle-dynamics modelling, J. Fluid Eng. 123 (2001) 359–371.
[29] B.E. Launder, N. Shima, Second-moment closure for near-wall sublayer: development and application, AIAA J. 27 (1989) 1319–1325.
[30] M. Wolfshtein, The velocity and temperature distribution in one-dimensional flow with turbulence augmentation and pressure gradient, Int. J. Heat Mass Transfer 12 (1969) 301–318.
[31] H.C. Chen, V.C. Patel, Near-wall turbulence models for complex flows including separation, AIAA J. 26 (1988) 641–648.
[32] R.I. Issa, Solution of the implicit discretized fluid flow by operator-splitting, J. Computat. Phys. 62 (1985) 40–65.
[33] B.P. Leonard, The ULTIMATE conservative difference scheme applied on unsteady one-dimensional advection, Comput. Methods Appl. Mech. Eng. 88 (1991) 17–74.
[34] E.R. Meinders, Th.H. van der Meer, K. Hanjalić, Application of infrared restoration technique to improve the accuracy of surface temperature measurements, in: Proceedings of Quantitative Infrared Thermography 3, EUROTHERM No. 50, Stuttgart, Germany, 1996, pp. 32–38.
[35] M.M. Gibson, B.E. Launder, Ground effects on pressure fluctuations in the atmospheric boundary layer, J. Fluid Mech. 86 (1978) 491–511.